Extended-x-ray-absorption-fine-structure investigation of mobile-ion density in superionic AgI, CuI, CuBr, and CuCl

J. B. Boyce, T. M. Hayes, and J. C. Mikkelsen, Jr.
Xerox Palo Alto Research Center, Palo Alto, California 94304
(Received 18 April 1980)

Extended-x-ray-absorption-fine-structure (EXAFS) data on the normal and superionic phases of AgI and the cuprous halides have been analyzed using four structural models: harmonic oscillator, displaced site, anharmonic oscillator, and excluded volume. The most satisfactory description is obtained with the last model, based upon a softened hard-sphere pair potential. The results indicate that the tetrahedral locations in the halogen lattice are preferred by the mobile cations, but that at elevated temperatures substantial cation density also occurs at bridging trigonal sites. For fcc immobile-ion lattices, significant octahedral occupation is also found at elevated temperatures. These results indicate that the likely conduction path between tetrahedral sites is in the ⟨110⟩ directions for bcc materials and in the ⟨111⟩ directions for fcc materials. The potential-energy barrier heights for conduction in various directions are obtained from the ion density. In addition, differences in the nature of the structural information probed by EXAFS and by diffraction techniques are discussed.

I. INTRODUCTION

Considerable experimental and theoretical effort has been devoted to understanding the behavior of superionic conductors. These materials are interesting in that they exhibit ionic conductivities comparable to those of molten salts while still in the solid phase [$\approx 1\ (\Omega\,\mathrm{cm})^{-1}$].[1] They include relatively simple binary salts like AgI (Refs. 2–11) and structurally complex ceramics like $Li_2Ti_3O_7$ (Ref. 12). Their ionic conductivities show different temperature dependences,[13] ranging from predominantly exponential behavior with a sharp discontinuity at a phase transition (as in AgI) to a continuous exponential increase over a wide temperature range (as in Na–β-Al_2O_3 and $Li_2Ti_3O_7$). The first category, dominated by Cu and Ag ion conductors, is particularly interesting since the onset of superionic conduction is associated with a true first-order phase transition, accompanied by changes in structure and discontinuities in the specific heat. The entropy increase at these solid-solid transitions is often half the entropy increase on melting of a normal salt—a fact which has led, in part, to the concept of sublattice melting at the transition.[14,15] AgI and the cuprous halides exemplify this behavior and are the materials we discuss in this paper. Selected information on the phases is listed in Table I.

At all temperatures in these salts, the halogen anions are closely bound to their lattice sites and

TABLE I. Selected information on the structures and phase transitions of AgI and the cuprous halides.

Material	Phase	Transition temperature (°C)	Structure	ΔS [J (mole K)$^{-1}$]
AgI	γ		Zinc blende (iodine fcc)	
	β		Wurtzite (iodine hcp)	
	α	147	Iodine bcc	14.5
	Melt	557		11.3
CuI	γ		Zinc blende (iodine fcc)	
	β	369	Iodine hcp	11.1
	α	407	Iodine fcc	4.7
	Melt	600		9.2
CuBr	γ		Zinc blende (Br fcc)	
	β	385	Br hcp	8.8
	α	469	Br bcc	3.8
	Melt	488		12.6
CuCl	γ		Zinc blende (Cl fcc)	
	β	407	Cl hcp	
	Melt	422		15.5

the cations are relatively mobile. As can be seen in Fig. 1, the ionic conductivity at low temperatures is well approximated by the Arrhenius expression

$$\sigma = \sigma_0/T \exp(-U/k_B T), \quad (1)$$

where T is temperature and U is the barrier height or activation energy. Just as one would expect for a normal salt, the conductivity is low [$<10^{-4}$ $(\Omega\,\mathrm{cm})^{-1}$] and is highly activated ($U \approx 1$ eV). In this normal phase, the cations are situated at well defined lattice sites and have very low mobility. They become much more mobile as the phase transition is approached. AgI is dimorphous at low temperatures, existing in either the wurtzite structure (β phase) or the zinc-blende structure (γ phase). The conductivity of both these phases is low, with the γ phase being a somewhat better conductor.[16] From either phase, the conductivity increases abruptly by a factor of 10^4 upon entering the superionic α phase at 147 °C (Ref. 17). The situation for the cuprous halides[18]

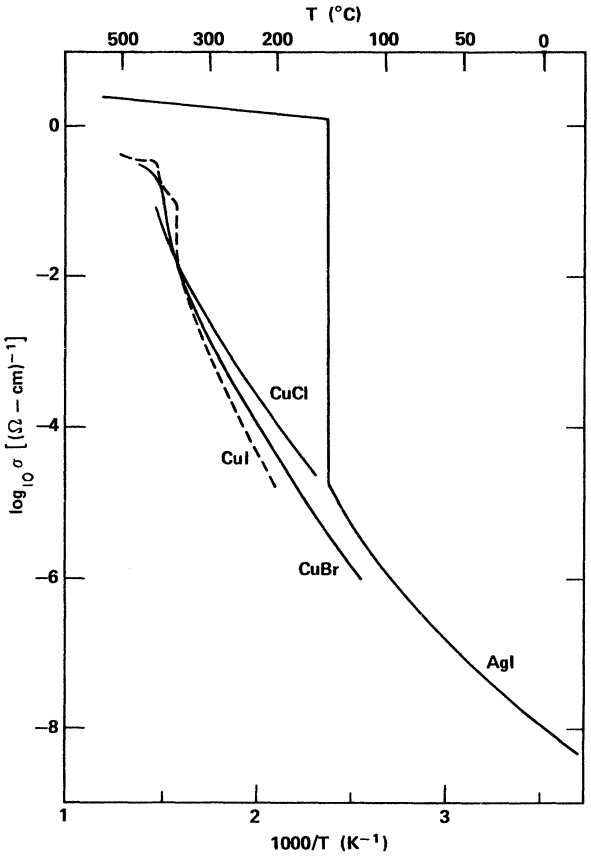

FIG. 1. Conductivity on a logarithmic scale versus inverse temperature for AgI (Refs. 16 and 17) and the cuprous halides (Ref. 18). Cationic conductivity dominates over this temperature region.

is different in that the conductivity increases more rapidly than exponential and achieves a large value [≈ 0.1 $(\Omega\,\mathrm{cm})^{-1}$] *below* the first phase transition. It increases further by a small factor at the two phase transitions $\gamma \rightarrow \beta$ and $\beta \rightarrow \alpha$. In each case, however, the α phases exhibit superionic behavior. That is, the cationic conductivity is large [≈ 1 $(\Omega\,\mathrm{cm})^{-1}$] and only slightly temperature dependent ($U \approx 0.1$ eV). (Although CuCl has no α phase, its conductivity is as substantial as that of CuBr and CuI at the high-temperature end of the γ phase and in the β phase.[18])

There is a latent heat at these phase transitions which corresponds to an entropy change $\Delta S \approx 10$ J $(\mathrm{mole\ K})^{-1}$ (Ref. 14). This is comparable to the entropy of fusion of these salts, as shown in Table I. The sum of these entropies is approximately equal to the entropy of fusion for normal salts [e.g., ≈ 24 J $(\mathrm{mole\ K})^{-1}$ for the alkali halides[14]]. This observation supports the concept of sublattice melting in superionic conductors. In this description, the transition to the superionic phase is viewed as a "melting" of the mobile-ion sublattice. This ionic liquid can flow readily through the rigid but relatively open immobile-ion sublattice. In these materials, the Ag or Cu sublattice melts while the halogen sublattice remains intact.

The characterization of these materials requires understanding the nature of the transitions to the superionic phase and of the motion of the cations that accounts for the high conductivity in this phase. Structural studies are particularly interesting in this regard to the extent that they can yield the location of the mobile ions relative to their immobile-ion nearest neighbors. From this information, it is possible to infer the conduction path as well as the nature of the cation disorder in the superionic phase. The structural information probed through the extended x-ray absorption fine structure (EXAFS) is especially useful in this respect. The EXAFS (Refs. 19 and 20) is the oscillations, as a function of photon energy, in the absorption cross section above the characteristic x-ray edges of an atom. These oscillations arise from an interference between the outgoing electron wave function and that small fraction of it backscattered from the near-neighbor atoms. It contains information on the near-neighbor environment of the excited atom only, and thus involves a subset of the pair-correlation functions probed in a diffraction experiment. This is a substantial simplification.

There are two significant additional differences in the nature of the information to be obtained from these two kinds of structural probes. Firstly, in x-ray- and neutron-diffraction studies of

superionic conductors, the complicated diffraction pattern contains both Bragg peaks from long-range order and a liquidlike diffuse scattering pattern from short-range correlations.[20,21] These two contributions are often dominated by the stationary lattice and the mobile-ion–mobile-ion correlations, respectively. The EXAFS on the cation K-shell absorption, on the other hand, measures primarily the pair-correlation function of the mobile cations with respect to the immobile anions. This correlation function is the most direct indicator of the conduction path. Secondly, to the extent that the mobile-ion–immobile-ion correlations *are* represented in the Bragg scattering of a diffraction measurement, the effect must be dominated by long-range correlations for low values of the scattering vector. The peaks at large r in the pair-correlation functions are significantly less sharp than those of nearest neighbors, due to the influence of long-wavelength acoustic phonons, certain types of static disorder, etc. In other words, the vibrative and diffusive motions of atoms separated by long distances are not preferentially in unison, unlike nearest neighbors. As a result, *if* the Bragg scattering for low values of the scattering vector is analyzed in terms of an effective nearest-neighbor distribution, it will yield a charge-density pattern which is artificially broad—and an apparent distance of closest approach which is unphysically short. While this charge density can yield some information about the cation conduction path through the crystal, it will yield little information about the short-range pairwise interactions which govern the conduction. The Bragg scattering for large scattering vectors ($q > 10$–15 Å^{-1}) could be analyzed to yield this information, but this is seldom done. In contrast, the EXAFS data bear directly on the *nearest-neighbor* contribution to the atom-atom correlation function, which *is* closely related to the conduction process. The effect of thermal vibrations on the EXAFS, as contrasted with the Debye-Waller treatment, has been discussed in the literature.[22] Owing to both of these differences, the EXAFS technique is especially well suited to determine the path taken by the conducting ions and to study the microscopic basis of the conduction process. This will be evident in the subsequent discussion of our results.

In the following, the results of EXAFS studies of AgI, CuI, CuBr, and CuCl are presented. The EXAFS data are analyzed in terms of a three-dimensional one-ion potential which determines the cation positions. This leads directly to a model which not only can explain the structural data but also can yield substantial insight into the details of the unusual ionic conduction in these materials. The experimental details are presented in Sec. II. In Sec. III are reviewed the underlying theory of the EXAFS and the data reduction process. Models for the structure of these materials are presented in Sec. IV. In Secs. V–VII are presented the experimental results and a discussion in terms of the various structural models. In Sec. VIII, the results are summarized and conclusions are drawn.

II. EXPERIMENTAL METHOD

A. Sample preparation

Samples were prepared from 99.999%-pure powders from Atomergic, New York. This high purity refers to the starting Cu or Ag metal. These as-received materials are usually somewhat contaminated with organic solvents used in washing the precipitated halides, and with water. The powders were outgassed and dehydrated in a vacuum drying oven at 140 °C before being sealed into silica ampoules. The cuprous halides were melted in one end of the ampoule and filtered through silica wool into the other end of the ampoule. A satisfactory alternative is to melt the material in air in the end of a test tube, and load the melt into an ampoule for filtering. Dark insoluble material often formed, probably CuO. Care was taken to avoid excess heating of the molten halide as it will dissolve the unwanted oxide. The small amount of cupric ions present was chemically reduced by the addition of high-purity copper metal to the melt. The final purification process of the cuprous halides included partial distillation and several sublimations. The resultant polycrystalline ingots were colorless CuCl, which has only slight light sensitivity, pale green CuBr, and faintly yellow CuI. AgI was purified in a similar manner, except that the distillation-sublimation was replaced by zone refining.

EXAFS samples were prepared from this starting material, with a slight loss of purity necessitated by the loading of the sample cells. The EXAFS cells are described in detail by Mikkelsen *et al.*[23] They are composed of inner pyrolytic boron nitride disks with a machined circular cavity for the sample. The cavity depth was chosen to obtain the desired sample thickness, which is discussed below. The cells were loaded with CuCl and CuBr by melting an excess of the salt into the cell cavity under flowing high-purity Ar. Agitation with a silica rod facilitated wetting and the complete filling of the cavity. The samples were cooled slowly to minimize cracking from thermal contraction, and were carefully

polished to the desired thickness, with a tolerance of about 3 μm. CuI and AgI tend to decompose in an open tube and could not be prepared in the above manner. CuI samples were ground to the correct thickness from polycrystalline ingots of the melted purified material. AgI-pressed pellets of the appropriate thickness were formed in a standard infrared sample press at 5000 psi. The disks were fragile and difficult to handle. The AgI was transformed to the low-temperature β phase by heating to 200 °C and cooling to room temperature.

B. Experimental apparatus and procedure

The experiments were performed at the Stanford Synchrotron Radiation Laboratory (SSRL) using the conventional experimental arrangement for an absorption experiment. The white radiation from the storage ring is passed through a double-crystal monochrometer, using an Si(111) crystal face for the experiments at the Cu K edge (8.98 keV) and Si(220) at the Ag K edge (25.5 keV). The intensity of this monochromatized radiation incident on the sample I_0 is monitored by a gas ionization chamber. The radiation then passes through the sample, and the transmitted intensity I is measured by a second chamber. These intensities are related by

$$I = I_0 \exp\left(-\sum_i \mu_i x_i\right), \tag{2}$$

where the sum includes all absorbing elements (of absorption coefficient μ_i and thickness x_i) in the path between the incident and transmitted counters. This includes the air, Dewar or furnace windows, sample holder, and sample. Absorption by other than the sample was kept to less than 20% to maximize signal-to-noise ratio. From considerations of statistics under the condition that the nonsample absorption is negligible, Kincaid[24] has shown that the maximal signal-to-noise ratio results from a sample thickness given by $\mu_s x_s \simeq 2.55$, where μ_s is the absorption coefficient of the sample just above the K edge of interest. This condition changes slightly when the nonsample absorption is significant. In our worst case of 20% nonsample absorption, the optimal sample thickness is reduced slightly to about $\mu_s x_s \simeq 2.50$ and the signal-to-noise ratio is reduced by 10%. The samples were thinned to approximately the optimal thickness: 125 μm of AgI for the Ag K edge, 29 μm of CuCl, 30 μm of CuBr, and 18 μm of CuI for the Cu K edge. The thickness criterion is rather broad so that small deviations from these thicknesses cause little deterioration in signal-to-noise ratio. In addition, the noise often seems to be dominated by factors other than the photon statistics which give rise to this criterion, such as synchrotron beam stability.

Another experimental factor is the gases used in the two proportional counters. Kincaid[24] determined the optimum absorption for the first counter, measuring I_0, to be $\mu_0 x_0 \approx 0.24$. Accordingly, we chose Ne ($\mu_0 x_0 \simeq 0.24$) at the Cu K edge and Ar ($\mu_0 x_0 \simeq 0.12$) at the Ag K edge for the 6-in.-long I_0 counter. The second counter, measuring I, was 12 inches long and the gas was chosen to absorb most of the transmitted photons: Ar ($\mu x \simeq 4.9$) at the Cu K edge and Kr ($\mu x \simeq 3.3$) at the Ag K edge.

For the low-temperature runs, the samples were kept within a few degrees of 77 K in a Dewar. For the elevated temperature runs, the furnace temperature was kept constant to within ±3 °C during the scan time of 15–30 min. A scan was performed at room temperature both before and after the runs at high temperatures. In all cases, these two room-temperature scans were identical, showing that no sample deterioration occurred at high temperatures. The intensities I_0 and I were recorded, along with the monochrometer position, using the standard SSRL equipment. The total absorptance $\ln(I_0/I)$ was obtained as a function of monochrometer angle θ or, equivalently, as a function of x-ray photon energy E, using Bragg's law: $E = hc(2d\sin\theta)^{-1}$. A typical such spectrum is shown in Fig. 2(a) for the case of CuI at 77 K in the region of the Cu K edge at 8.98 keV. The EXAFS is evident as sharp oscillations in the absorption cross section extending for about 1000 eV above the edge. The two sharp peaks in this cross section just above the edge are not part of the EXAFS but rather are the "white lines," arising from either a high density of final states or the substantial overlap of an unusually localized final-state wave function with the K shell.[25] We now discuss the EXAFS theoretical expressions and data reduction procedure used to extract the structural information from the spectrum.

III. EXAFS DATA ANALYSIS

The theoretical basis used to extract structural information from the EXAFS has been discussed extensively in the literature.[19,20,26–33] We review the salient features here for K shell absorption. The total absorption coefficient obtained from Eq. (2) is

$$\mu = \mu_K + \mu_{\text{background}}, \tag{3}$$

where μ_K is the sample absorption for the K shell of interest and $\mu_{\text{background}}$ is all other absorption,

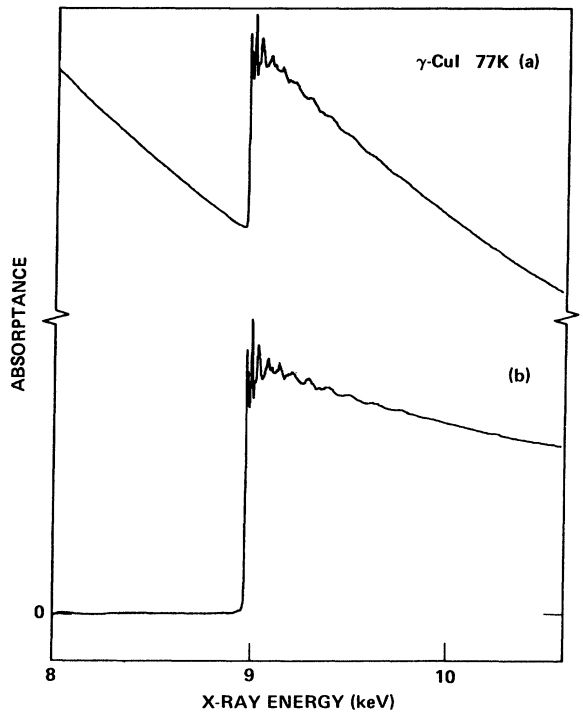

FIG. 2. (a) The absorptance of CuI at 77 K as a function of x-ray photon energy in the region of the Cu K edge at 8.98 keV. (b) The Cu K-edge absorptance obtained from (a) after removal of the background described by Eq. (4) with $p = 1.65$.

including that from other atoms in the sample and lower-energy edges of the atom of interest (L edge, ...) as well as the absorption from sample cell, windows, etc. times the ratio of effective thicknesses. Such a total absorption for CuI is shown in Fig. 2(a). An essential feature is that the background absorption is smoothly varying with photon energy since this region is far from any other characteristic absorption edges. In that case, the background absorption falls off with energy approximately as

$$\mu_{\text{background}} = A + BE^{-p}, \tag{4}$$

where A, B, and p are determined by a least-squares fit to the data below the K edge of interest. In practice, p is found to be between 1 and 3, consistent with the often-used Victoreen formula.[34] The background absorption is then subtracted from the total, yielding μ_K. The result of such a procedure is shown in Fig. 2(b) for the Cu K-edge absorption of CuI at 77 K, where the fit range was from 1000 to 100 eV below the K edge. In this case, a value of $p = 1.65$ gave the best fit below the threshold.

The resulting μ_K consists of two parts, the atomiclike K-shell absorption μ_K^0 and the EXAFS $\Delta(k)$, according to

$$\mu_K = \mu_K^0[1 + \Delta(k)]. \tag{5}$$

The EXAFS depends on the final-state electron momentum k given by

$$\hbar^2 k^2/2m = E - E_0, \tag{6}$$

where E_0 is the binding energy of the K-shell electron. To extract $\Delta(k)$, the kinetic energy zero of the photoexcited electron E_0 has to be determined and μ_K^0 has to be removed. E_0 is taken to be the photon energy at which the absorption μ_K is half of its maximum value, excluding the white line. For CuI in Fig. 2(b) this is 8982.6 eV. If this does not correspond to the true zero of kinetic energy of the photoexcited electron, then there will be a systematic distortion of the k scale according to Eq. (6). Since the E_0 for the standard and for the unknown are chosen in the same manner, this distortion should not affect comparisons between the data sets. This is particularly true when the structural standard and the unknown are similar, as they are in this study, where the standard used is the actual sample at low temperatures (77 K).

The second step in extracting $\Delta(k)$ is the removal of μ_K^0. This is accomplished by fitting μ_K above the edge to a fourth- or sixth-order polynomial in k. Such a function is slowly varying compared with the EXAFS so that only the smooth μ_K^0 is fit. The fit range in the case of CuI at 77 K extends from about 15 eV above E_0 to the end of the data set, approximately 1500 eV above the edge. One then divides μ_K by this fit, subtracts one, and converts the E scale to a k scale to obtain $\Delta(k)$. The resulting EXAFS for CuI at 77 K is shown in Fig. 3(a).

The EXAFS $\Delta_\alpha(k)$ on the K-edge of atom species α may be written as[30]

$$k\Delta_\alpha(k) = \sum_\beta \int_0^\infty \frac{dr}{r^2} p_{\alpha\beta}(r) 2\,\mathrm{Re}[\exp(2ikr)\Lambda_{\alpha\beta}(k,r)], \tag{7}$$

where

$$\Lambda_{\alpha\beta}(k,r) \simeq -2i\pi^2 t_\beta(k) \exp[-2r/\lambda(k) + 2i\delta_\alpha(k)]. \tag{8}$$

The EXAFS is divided into two parts. The structural information is in $p_{\alpha\beta}(r)$, while the details of the electron scattering processes are contained in Λ. $p_{\alpha\beta}(r)$ is the pair-correlation function of β atoms about the excited atom α. It is normalized so that $\int dr\, p_{\alpha\beta}(r)$ is the total number of β atoms in the sample. The sum over β in Eq. (7) includes all the atom species in the sample. Λ contains the electron backscattering t matrix for the neighboring β atoms $t_\beta(k)$, the electron mean free path $\lambda(k)$, and the $l = 1$ phase shift due to the po-

tential of the excited α atom $\delta_\alpha(k)$. Equation (7) applies to polycrystalline materials where the dependence on the angle between the photon polarization and the vector joining atoms α and β averages to a constant.

The simplest peak in a pair-correlation function is a Gaussian, which describes the case for harmonic vibrations about the lattice sites. Consider one shell of β neighbors containing N_β atoms at a distance r_β from the excited atom α. Then, suppressing the subscript α,

$$p_{\alpha\beta}(r) = N_\beta (2\pi\epsilon_\beta^2)^{-1/2} \exp[-(r-r_\beta)^2/2\epsilon_\beta^2], \quad (9)$$

where ϵ_β is the rms deviation in the atomic spacing about the mean r_β. Since $p_{\alpha\beta}(r)$ is sharply peaked at r_β for this case, Eqs. (7) and (8) simplify to the widely-used expression

$$k\Delta_\alpha(k) \simeq N_\beta r_\beta^{-2} |t_\beta(k)| \times \exp(-2r_\beta/\lambda - 2k^2\epsilon_\beta^2) \sin(2kr_\beta + 2\delta_\alpha + \delta'_\beta), \quad (10)$$

where δ'_β is the phase shift from the t matrix of the backscattering atom. This expression shows that the EXAFS is a sum of sinusoids with different frequencies for each shell of neighbors, as can be seen in Fig. 3(a). Figure 3(b) shows the Fourier-filtered data for the first shell only of iodine neighbors. This procedure, discussed below, picks out the contribution of a given shell of neighbors from Eq. (7). This sinusoid is damped by thermal broadening effects and further modified by the k-dependent t matrix. For a heavy-atom backscatter, as is the case here, $t(k)$ is particularly complicated, including a phase change of π near $k = 6$ Å^{-1} as seen in Fig. 3. It should be mentioned that the first two peaks of Fig. 3(a), below 2 Å^{-1}, are the resonances discussed above, not EXAFS. As a result, the low-k information is lost to the EXAFS, as shown explicitly in the Fourier-filtered data of Fig. 3(b).

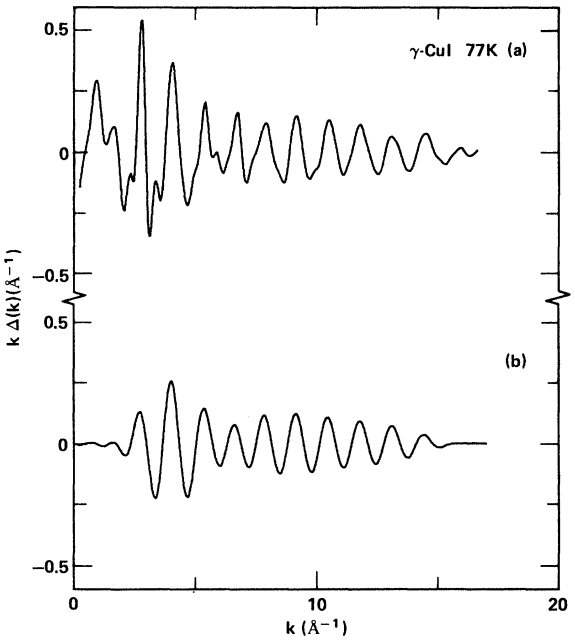

FIG. 3. (a) The EXAFS oscillation $k\Delta(k)$ on the Cu K-edge absorption in CuI at 77 K as a function of photoelectron momentum k after removal of the background and atom-like absorption. (b) The Fourier-filtered EXAFS that corresponds to the first shell of iodine atoms about the Cu for CuI at 77 K. This is obtained by Fourier transforming (a) into real space using a k-space window from 2.85 to 13.6 Å^{-1}, Gaussian broadened by 0.7 Å^{-1}. The resulting real space data [see Fig. 4(a)] are back transformed into k space using a window that contains only the first peak, namely, 1.4–3.4 Å, Gaussian broadened by 0.2 Å.

The various shells of neighbors can often be resolved from one another in r space.[26] A Fourier transform of Eq. (7) yields[30]

$$\varphi_\alpha(r) = \sum_\beta \int_0^\infty \frac{dr'}{r'^2} p_{\alpha\beta}(r') \xi_{\alpha\beta}(r - r'), \quad (11)$$

where the peak function $\xi_{\alpha\beta}(r)$ is the Fourier transform of $\Lambda_{\alpha\beta}(k)$ over the limited k range of the data. In essence, φ is a linear combination of ξ's, one located at the position of each peak in p. Figure 4(a) shows an example of $\varphi(r)$, derived

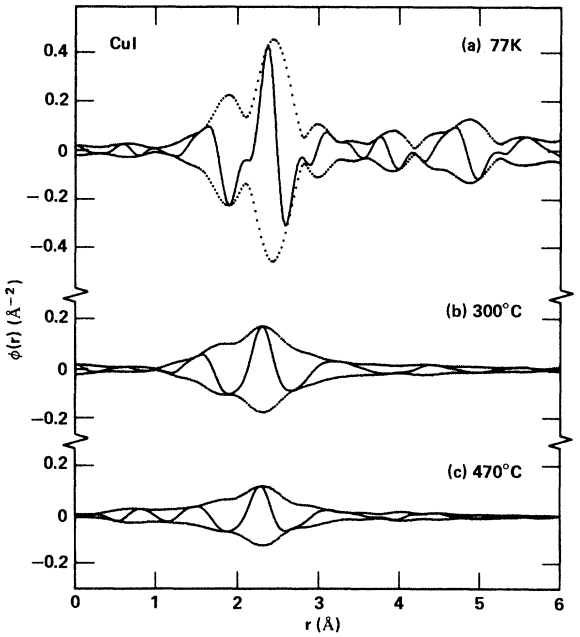

FIG. 4. Real part (solid line) and the magnitude of the Fourier transform of the EXAFS on the Cu K edge in CuI (a) at 77 K, (b) at 300 °C in the high-temperature end of the γ phase, and (c) at 470 °C in the superionic α phase. The window used for the transform is $k = 2.85$–13.6 Å^{-1}, Gaussian broadened by 0.7 Å^{-1}.

from the Cu K-shell absorption in CuI at 77 K. The transform window is 2.85–13.6 Å^{-1}, broadened by a Gaussian width of 0.7 Å^{-1}. The double-peaked structure at approximately 2.2 Å is the signal from a single shell containing the four iodine neighbors to each Cu atom in this zinc-blende structure. $\xi_{\text{Cu-I}}$ is double peaked due to a Ramsauer-Townsend[35] resonance in the iodine backscattering t matrix, also responsible for the phase shift near $k=6$ Å^{-1} discussed above (Fig. 3). The next two peaks are due to the Cu second neighbors and the iodine third neighbors, respectively. The first-neighbor peak dominates the spectrum due mainly to the fact that thermal broadening effects are larger for further neighbors, but also to the r^{-2} factor of Eqs. (7), (10), and (11). The larger thermal broadening for the third neighbor can be seen in the decreased height of the third peak compared with the first peak of Fig. 4(a). The positions of the peaks in Fig. 4(a) are shifted inward from the actual near-neighbor spacing due to the k dependence of the phase shift $[2\delta_\alpha(k)+\delta'_\beta(k)]$ in Eq. (10), or, equivalently, due to the fact that $\xi(r)$ peaks at $r\simeq -0.16$ Å.

The first peak in $\varphi(r)$ is resolved from the others and so can be analyzed separately, either in r space, Fig. 4(a), or in k space, Fig. 3(b). An additional Fourier transform is required for k-space studies and the transform range used to obtain the filtered data of Fig. 3(b) is 1.4–3.4 Å, Gaussian broadened by 0.2 Å. Analysis of the k-space data [Fig. 3(b)] or of the first-neighbor peak of the r-space data [Fig. 4(a)] should yield equivalent results, depending upon the details of the analysis. For these studies, we have chosen to analyze the r-space data using Eq. (11).

The first peak is the one of interest for the studies presented here since it yields the location of the mobile cations relative to the immobile anion lattice. In fact, only the first peak is observed with adequate signal-to-noise ratio at elevated temperatures, as can be seen in Figs. 4(b) and 4(c). These are the r-space data on the Cu K edge of CuI at 300 °C in the high-temperature end of the γ phase [Fig. 4(b)], and at 470 °C in the superionic α phase [Fig. 4(c)]. The sample and the data reduction procedure are the same as for Fig. 4(a). The $\varphi(r)$'s differ substantially, however, with the first-neighbor peak being broader and reduced in amplitude at the higher temperature. In addition, it has shifted inward by about 0.12 Å despite the fact that lattice expansion has caused an increase of 0.03 Å in the Cu–I near-neighbor spacing. Since ξ is insensitive to crystal structure, local bonding, thermal effects, etc.,[32,36] the changes that are observed between Figs. 4(a), 4(b), and 4(c) are due entirely to changes in $p(r)$ with temperature. The narrow, symmetric Gaussian $p(r)$ of 77 K [Fig. 5(a)] becomes broad and asymmetric at 300 °C [Fig. 5(b)] and 470 °C [Fig. 5(c)].

We quantify these changes in the following manner. Since $p_{\alpha\beta}(r)$ is a narrow Gaussian of known position at low temperatures in these materials, the unchanging ξ may be extracted using Eq. (11) from the $\varphi(r)$ measured at 77 K. This $\xi(r)$ can then be used to determine the unknown $p(r)$ at elevated temperatures. This is accomplished by formulating a model for $p(r)$. From the model $p(r)$ and the $\xi(r)$ obtained from the low-temperature data, one can calculate a model $\varphi_m(r)$ using Eq. (11). One can then compare $\varphi_m(r)$ with the data and adjust the model parameters using a least-squares criterion. The parameter which is minimized is

$$R=(2N)^{-1}\sum^{N}\left\{\mathrm{Re}(\varphi-\varphi_m)^2\Big/\left[(\mathrm{Re}\varphi)^2+\left(\mathrm{Re}\frac{d\varphi}{dr}\right)^2\right]+\mathrm{Im}(\varphi-\varphi_m)^2\Big/\left[(\mathrm{Im}\varphi)^2+\left(\mathrm{Im}\frac{d\varphi}{dr}\right)^2\right]\right\}, \tag{12}$$

where the sum is over the N data points in the

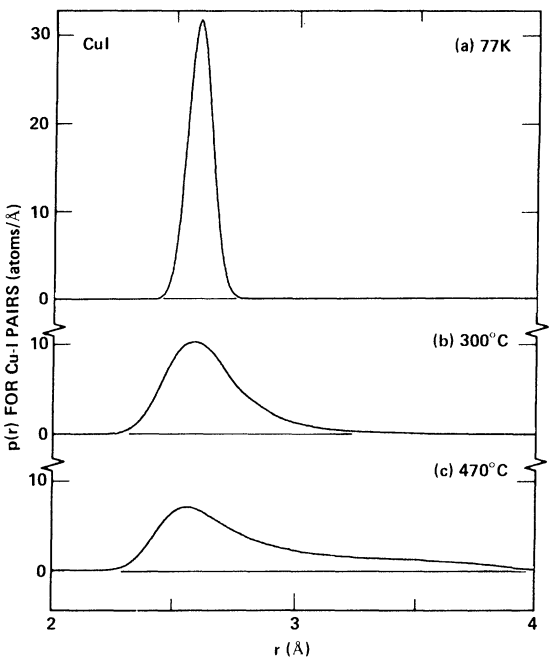

FIG. 5. First-neighbor pair correlation function for CuI (a) at 77 K, (b) at 300°C, the high-temperature end of the γ phase, and (c) at 470 °C in the superionic α phase. Part (a) is a Gaussian of width 0.06 Å, while (b) and (c) are obtained using the excluded-volume model as described in Secs. III–V.

range of the spectral feature of interest. This is a weighted fractional difference least squares, where the $d\varphi/dr$ term has been added to enhance the sensitivity of R to variations in the shape of $p(r)$ at the expense of some of its great sensitivity to position. This procedure yields an optimal set of parameters for a particular model $p(r)$. One then repeats this process for other physically realistic models for $p(r)$. If the various models yield R values which are substantially different, then one may conclude that the EXAFS contains sufficient information to choose among the structural models. This is the case for the superionic conductors as will be discussed below.

Use of a model is essential in obtaining $p(r)$ from Eq. (11) because the EXAFS is lacking some information.[30,37,38] The low-k components of $p(r)$ are missing due to the presence of the resonances at low k that dominate the EXAFS, due to multiple scattering at low k and, for many backscatterers, due to the small value of the t matrix at low k. As a result, the lower limit on k-space information is typically 2–3 Å^{-1}. Also, the high-k information (beyond about $k=20$ Å^{-1}) often cannot be obtained due to thermal broadening effects as well as the falloff with k of $t(k)$. These k-space limits are evident in the Fourier-filtered data of Fig. 3(b). As a result, one must model $p(r)$ to allow a meaningful extrapolation into the low-k and high-k regions, where data is lacking.

It should be mentioned that the structural information is obtained straightforwardly from Eq. (10) or (11) if the Gaussian model for $p(r)$ is appropriate. This model is valid, however, only for harmonic materials. The narrow symmetric Gaussian $p(r)$ becomes broad and asymmetric for anharmonic systems (see Fig. 5). The superionic conductors are indeed very anharmonic since the ions not only vibrate vigorously about an equilibrium site but also actually hop from one site to another. So a simple Gaussian is not appropriate for the superionic materials, as is shown in Secs. V–VII, and a more complicated pair-correlation function has to be determined. The models used for $p(r)$ are discussed in the next section.

IV. STRUCTURAL MODELS

To provide a frame of reference for the discussion of the EXAFS data, we first discuss the various models which have been proposed to explain structural data on the superionic conductors. The simplest approach is to model $p(r)$ directly. For example, it could be assumed that the nearest-neighbor contribution to $p(r)$ is a single Gaussian peak: a harmonic model. Such a $p(r)$ results from the harmonic approximation to the ion potential and corresponds to the cations being located in a site that is equidistant from the neighboring anions and executing symmetric, harmonic vibrations about this site. Slightly more sophisticated are the displaced site models, in which the cations in the high-temperature superionic phase are assumed to be statistically distributed over metastable sites which are displaced from the central site in certain symmetry directions (e.g., along probable conduction paths). For example, in low-temperature γ-CuI the Cu ions occupy the tetrahedral sites but, in the spirit of this model, are displaced in superionic α-CuI along $\langle 111\rangle$ directions toward the faces of the tetrahedra. Such models have been applied to AgI,[5,6,8,11] CuI,[39–41] CuBr,[40,42,43] and CuCl.[43–45] They are somewhat successful since they yield an asymmetric near-neighbor pair-correlation function, which is needed to fit the structural data. They can be criticized, however, on the grounds that they are phenomenological, static, and often yield small displacements comparable to vibration amplitudes.[6] One would expect a dynamic model to be more appropriate since the ions are mobile. In addition, we have tested these models using our EXAFS data on AgI (Refs. 46 and 20) and the cuprous halides,[20,41,43] and find they are inferior to an excluded-volume model, as will be discussed.

A more general approach to formulating a structural model begins by defining a microscopic potential $V(\vec{r})$ in which the cations move. The ion density follows directly from this potential through the Boltzmann relation:

$$\rho(\vec{r})=\rho_0\exp[-V(\vec{r})/k_BT]. \tag{13}$$

The problem of modeling the structure has become one of modeling the potential. It is possible to use a very general form for the ion-ion pair interaction, which would include the core-core repulsion, Coulomb interaction, and ionic polarizabilities:

$$V_{ij}(\vec{r})=A_{ij}\exp\left(\frac{r_i+r_j-r}{\delta_0}\right)+\frac{q_iq_je^2}{r}-\tfrac{1}{2}(\alpha_iq_j+\alpha_jq_i)\frac{e^2}{r^4}. \tag{14}$$

The first term is the overlap repulsion between closed-shell ions, where r_i is the radius of the ith ion and $\vec{r}$ is the vector joining ions i and j. The second term is the Coulomb potential, where q_i is the fraction of ionic charge. The third term is the polarization self-energy of the ions, where α_i is the ionic polarizability. This approach has been taken in various calculations, including the molecular dynamics simulations[47] and calculations of the potential energy of ions of varying size in

the α-AgI lattice by Flygare and Huggins.[48] It is very cumbersome, however, in analyzing structural data, leading to the use of much simpler models for the potential. We will now discuss two of these, the anharmonic and excluded-volume models.

In the anharmonic models, the ions are assumed to be independent oscillators and the potential is expanded about an equilibrium position. This approach yields ionic potentials of the form

$$V(\vec{r}) = V_0 + \tfrac{1}{2}a_1(x^2+y^2) + \tfrac{1}{2}a_2 z^2 + \tfrac{1}{2}b(x^2-y^2)z + \cdots , \tag{15}$$

where $\vec{u} = (x, y, z)$ is the displacement of the ions from this equilibrium site and V_0, a_1, a_2, and b are constants. The precise form of the terms in Eq. (15) depends on the lattice symmetry. The form shown is for the distorted tetrahedral site of a bcc lattice,[11] that appropriate, for example, for Ag in α-AgI and for Cu in α-CuBr. For the tetrahedral site of an fcc lattice, the anharmonic potential is

$$V(\vec{r}) = V_0 + \tfrac{1}{2}au^2 + \tfrac{1}{2}bxyz + \cdots . \tag{16}$$

This form is appropriate for Cu in the fcc iodine lattice of γ- and α-CuI. If the anharmonic terms are negligible, then Eqs. (13) and (16) lead to a Gaussian pair-correlation function with a width $\epsilon \approx (k_B T/a)^{1/2}$. If the anharmonic terms are non-negligible, the pair-correlation function becomes asymmetric, similar to the shape required by the structural data. Therefore, this model has been somewhat successful for AgI,[6,9,11] CuI,[41,49] CuBr,[43,50] and CuCl.[43-45,51] One expects an expansion about the equilibrium site of the form of Eqs. (15) and (16) to break down, however, for the superionic conductors where a cation must leave one equilibrium site and hop to another. An indication that this is the case is found in the neutron-diffraction work on AgI by Cava *et al.*,[9] who find that significant fourth-order terms must be included in the anharmonic expansion of the potential. In addition, we have tested the anharmonic model with cubic terms only and find it to be inferior to another approximation to the potential, the hard-sphere approximation which we now discuss.

The excluded-volume model[46] for $V(\vec{r})$ assumes that the hard-core repulsion dominates the ion-ion interaction:

$$V_{ij}(\vec{r}) = \begin{cases} \infty, & r < r_i + r_j = r_{\text{excluded}} \\ 0, & r > r_i + r_j = r_{\text{excluded}} \end{cases} \tag{17}$$

with r_i the effective hard-sphere radius of atom i. The anions are fixed at their lattice sites and only cation-anion interactions are considered. The cation density is then a constant ρ_0 *except* that it is zero within a distance of r_{excluded} of an anion site, where $r_{\text{excluded}} = r_c + r_a$, the effective hard-sphere radii of cation and anion. For one anion at the origin, the cation density $\rho_c^1(\vec{r})$ is given by

$$\rho_c^1(\vec{r}) = \begin{cases} 0, & r < r_{\text{excluded}} \\ \rho_0, & r > r_{\text{excluded}} \end{cases} . \tag{18}$$

While Eq. (18) is appropriate for a hard-core interaction, the actual interactions have a finite slope, or softness, and the anions are known to execute large amplitude vibrations about their lattice sites. To account for these effects we convolute Eq. (18) with a Gaussian of width ϵ. The density can then be expressed in terms of the complementary error function as

$$\frac{\rho_c^1(\vec{r})}{\rho_0} = \begin{cases} \operatorname{erfc}(x)/2, & r < r_{\text{excluded}} \\ 1 - \operatorname{erfc}(x)/2, & r > r_{\text{excluded}} \end{cases} \tag{19}$$

where $x^2 = (r - r_{\text{excluded}})^2/2\epsilon^2$. To obtain the total cation density $\rho_c(\vec{r})$ one must include the effect of all the anion near neighbors, located at $\vec{r}_j$. Equation (19) is then generalized to yield

$$\rho_c(\vec{r}) = \rho_0 \prod_j^N \frac{\rho_c^1(\vec{r} - \vec{r}_j)}{\rho_0} , \tag{20}$$

where the product includes all the N anion sites in the crystal. From this cation density, the cation-anion pair-correlation function $p_{c-a}(r)$ can be calculated as follows:

$$p_{c-a}(r) = 4\pi r^2 N^{-1} \sum_j^N \langle \rho_c(\vec{r} + \vec{r}_j) \rangle_{\Omega_r} . \tag{21}$$

In fitting the EXAFS data using Eq. (21), the lattice of the anions is determined from diffraction results. Only the two parameters r_{excluded} and ϵ need be adjusted to determine the cation-anion pair-correlation function in many systems.

In the fcc and hcp phases of these materials, however, an additional parameter must be added. One can distinguish two types of voids for the cations, tetrahedrally and octahedrally coordinated sites. In the fcc halide lattice at low temperatures, only alternate tetrahedral voids are occupied. As the temperature is increased, however, the octahedral occupation is expected to increase since the conduction path for motion through the faces of the polyhedra will consist of alternating tetrahedral and octahedral sites.[52] Since the near-neighbor environment is different for Cu ions in these two sites, their relative occupation will be determined by interactions in

addition to the softened hard-sphere repulsion. These can be treated phenomenologically by superimposing on $V(\vec{r})$ a square-well potential which is zero in the tetrahedral location and greater than zero in the octahedral location. This square-well potential gives the correct low-temperature structure. Its temperature variation determines how the relative occupation of the two sites changes as one approaches the superionic phase. Accordingly, a third parameter is introduced in fitting the cuprous halide data, the fraction of Cu ions found in the octahedral sites c_{oct}. The near-neighbor $p_{c-a}(r)$ for these materials will consist of the sum of two parts: a tetrahedral contribution with four halide ions around a Cu ion, weighted by $c_{tet} = (1 - c_{oct})$ and an octahedral contribution with six halide ions around a Cu ion, weighted by c_{oct}. The three parameters, $r_{excluded}$, ϵ, and c_{oct}, are adjusted to fit the data. We now consider the experimental results on these superionic conductors, and the ability of the various models to explain the data.

These various structural models have been tested against EXAFS data using the procedures discussed in Sec. III. Wherever possible, we have compared our results directly with the results of diffraction studies. As is to be expected on the basis of the discussion in the Introduction, the near-neighbor distribution inferred from measurements of Bragg scattering is *always* much too broad to explain the EXAFS data. This is properly ascribed to fundamental differences in the structural information probed in the two measurements. Bragg scattering is dominated by long-range correlations. As a consequence, charge-density distributions determined from it will have vibrational components which are too large to properly represent a nearest-neighbor distribution. In contrast, the EXAFS data bears directly on the nearest-neighbor distribution. We now consider each of the materials separately.

V. EXPERIMENTAL RESULTS AND DISCUSSION FOR AgI

The EXAFS on the Ag K edge in AgI was measured as a function of temperature from 77 K in the low-temperature β phase up into the superionic α phase.[8,46] The 77-K data on β-AgI served as the structural standard. At this temperature the Ag ions are at the center of an iodine tetrahedron in the wurtzite structure, so that the near-neighbor Ag–I pair-correlation function $p_{Ag\text{-}I}(r)$ is a narrow Gaussian centered at 2.81 Å with $N = 4$ neighbors. The width is somewhat uncertain but is typically ≈ 0.06 Å. Various structural models for the superionic α phase were tested. We summarize the results using the data on α-AgI at 198 °C.

(1) For a single Gaussian harmonic model, the number of iodine neighbors N, the Ag–I nearest-neighbor spacing r_0, and the Gaussian width ϵ were adjusted to fit the data by minimizing R. This model did not fit very well, yielding $R = 4.5\%$ with $r_0 = 2.81$ Å and $N = 2.72$ neighbors (see Table II). Although the value of r_0 is very

TABLE II. Parameters obtained for several structural models when adjusted to fit the data on superionic AgI and CuI. The uncertainty in the determined distances is 0.01 Å and in the other parameters is ≈10%.

Material	Model	R (%)	N	r_0 (Å)	ϵ (Å)
α-AgI	Tet. site		4	2.83	
198 °C	Harmonic	4.5	2.7	2.81	0.13
	Strock	11.9	(see text)		
	Displaced site:	4.2	1.28	2.74	0.09
	⟨100⟩		1.28	2.88	0.09
	Displaced site:	3.1	1.95	2.77	0.10
	⟨110⟩		0.65	2.93	0.10
	Anharmonic	3.6	(see text)		
	Excluded volume	2.0	($r_{excluded} = 2.69$)		
α-CuI	Tet. site		4	2.67	
470 °C	Oct. site		6	3.08	
	Harmonic	6.9	4	2.59	0.20
		3.5	2.2	2.57	0.14
	Displaced site:	7.9	3	2.54	0.17
	⟨111⟩		1	3.21	0.27
		4.2	3	2.59	0.17
			1	3.15	0.29
	Anharmonic	4.6	(see text)		
	Excluded volume	1.8	($r_{excluded} = 2.44$, $c_{oct} = 30\%$)		

close to the value of 2.83 Å for the center of the tetrahedral site, the amplitude is reduced from the 4 expected for that site.

(2) The Strock model[2] distributes the two Ag ions uniformly over the 42 crystallographic sites in the unit cell formed by the bcc iodine ions. These 42 sites consist of 12 tetrahedral, 6 octahedral, and 24 trigonal locations. $p_{\text{Ag-I}}(r)$ in this case is a sum of Gaussians corresponding to each of the three types of sites: $r_0 = 2.83$ Å and $N = 4$ for the tetrahedral site, $r_0 = 2.69$ Å, $N = 3$ for the trigonal site, and $r_0 = 3.57$ Å, $N = 4$ plus $r_0 = 2.53$ Å, $N = 2$ for the distorted octahedral site. These Gaussians were weighted by the degeneracy of the sites. The widths were assumed to be equal, and adjusted for a best fit to the data. This model did not fit well, yielding $R = 11.9\%$.

(3) For the displaced-site model, displacements in two different directions from the tetrahedral site have been considered: ⟨100⟩ and ⟨110⟩.

(a) For a ⟨100⟩ displacement, the Ag ions are moved from the tetrahedral center toward octahedral sites. $p_{\text{Ag-I}}(r)$ is the sum of two Gaussians, centered at r_1 and r_2 and each having the same amplitude ($N = 2$) and the same width. Buhrer and Halg[5] proposed such a model with a displacement of 0.29 Å at 195 °C corresponding to $r_1 = 2.72$ Å and $r_2 = 2.97$ Å. This particular displacement did not fit the EXAFS data ($R = 13.1\%$). By allowing r_1 and r_2 to vary, the fit improved somewhat but still did not reproduce the data well. If the amplitude is allowed to vary in addition, the fit improves substantially to $R = 4.2\%$ for the parameters shown in Table II. Note that the EXAFS data leads to a displacement of 0.14 Å, one-half the result of the diffraction study.[5] This corresponds to a substantially more narrow nearest-neighbor distribution, as expected on the basis of previous discussion. The reduced amplitude (2.56 neighbors in all instead of 4) and the rather high R indicate that this model does not yield a good approximation to $p_{\text{Ag-I}}(r)$.

(b) For a ⟨110⟩ displacement, the Ag ions are moved from the center of the tetrahedral sites toward the faces of the tetrahedra, the trigonal sites. This is a likely displacement for Ag ion conduction between tetrahedral locations, through the shared faces.[52] In this case, $p_{\text{Ag-I}}(r)$ is the sum of two Gaussians with amplitudes in the ratio[8] of 3 to 1 (since this displacement moves an Ag ion closer to the three iodine ions of the tetrahedral face and further from the one iodine ion at the tetrahedral corner). If the amplitudes were fixed at $N_1 = 3$ and $N_2 = 1$, then the fit was not good. If the amplitudes were allowed to vary with the ratio fixed at 3:1, then the fit improved substantially to $R = 3.1\%$ with the parameters shown in Table II. This fit corresponds to a reduced amplitude of 2.60 neighbors instead of 4.

(4) For the anharmonic model, the proper form for the potential acting on an Ag ion vibrating about a distorted tetrahedral site in the bcc iodine lattice of α-AgI is given by Eq. (15). It has been used by Hoshino *et al.*[11] to describe their diffraction data, resulting in the following values for the parameters at 250 °C: $a_1 = 0.26 \times 10^{-12}$ erg Å^{-2}, $a_2 = 0.92 \times 10^{-12}$ erg Å^{-2}, $b = 3.47 \times 10^{-12}$ erg Å^{-3}. These parameters did not fit the EXAFS data ($R = 34\%$) because the potential is too soft, yielding a nearest-neighbor distribution which is too broad. If the potential parameters are allowed to vary to minimize R, they increase by a factor of 4 and R improves to 3.6%. This halves the width of the nearest-neighbor distribution, consistent with the earlier discussion. Even this stiffer anharmonic model, however, does not explain the EXAFS data adequately. The cubic terms are just not a sufficiently strong departure from the harmonic model. The model could be improved by adding still higher-order terms, as did Cava *et al.*,[9] or a more radically anharmonic model could be used—the excluded-volume model.

(5) In the excluded-volume model, the Ag ions are distributed uniformly over all the allowed space in the iodine bcc lattice, being excluded only from a region about the iodine ions described by the softened hard-sphere interaction.[46] The largest such allowed void is the tetrahedral location. The amplitude of $p_{\text{Ag-I}}(r)$ is completely determined in this model since one includes all four iodine nearest neighbors in Eq. (21). Specifying that the iodine ions form a bcc lattice with $a_0 = 5.068$ Å at 200 °C,[5] the two parameters r_{excluded} and ϵ were adjusted for a best fit to the EXAFS data at 198 °C. This model yielded a good fit with $r_{\text{excluded}} = 2.69$ Å and $\epsilon = 0.08$ Å ($R = 2.0\%$), substantially better than the results of the other models considered ($R > 3.1\%$). An example of this fit is shown in Fig. 6. The data is shown in Fig. 6(a) with the excluded-volume model simulation in Fig. 6(b) over the r space range of the fit. The difference between the data and simulation is presented in Fig. 6(c) and corresponds to a deviation of $R = 2.0\%$. Similarly good fits were obtained for the data at all the other temperatures studied.

No reduction in the amplitude of $p_{\text{Ag-I}}(r)$ is required for this model. It yields the correct amplitude, a total of four neighbors for the tetrahedral sites. It should be noted that only the tetrahedral and trigonal locations have substantial occupation in the superionic α phase since their Ag–I near-neighbor spacing is greater than r_{excluded}. The octahedral location, on the other

hand, has its near-neighbor spacing less than r_{excluded} and so has substantially less occupation than the other sites. It should be noted that an additional constraint was added in applying this model to the wurtzite β phase: that the ions do not occupy the octahedral sites. This is undoubtedly a valid assumption due to the small conductivity and low disorder in this phase. No such constraint was applied to the superionic phase, where the Ag ions are permitted to occupy all the voids in the bcc iodine lattice allowed by the hard-core repulsion.

These structural results can yield some insight into the conduction process and the transition to the superionic phase. Fig. 7(a) shows the temperature variation of both r_{excluded} and r_{face}, that value of r_{excluded} which corresponds to the allowed volume just touching the face of the tetrahedral cage, as determined from the lattice constant. For example, $r_{\text{face}} = 0.530 a_0$ in the bcc α phase. It is seen that $r_{\text{excluded}} > r_{\text{face}}$ in the normal β phase, so that the Ag ions are confined to the central region of the tetrahedral site. Furthermore, the tetrahedra share faces only in pairs in this wurtzite structure, and so an Ag ion would have to move into an octahedral site to move any distance through the hexagonal iodine lattice. Cation conductivity requires an activated hop between allowed volumes. As a result, the ionic conductivity is expected to be small and highly activated, as observed ($U = 0.96$ eV).[16,17] In the α phase, however, r_{excluded} is less than r_{face}. Fur-

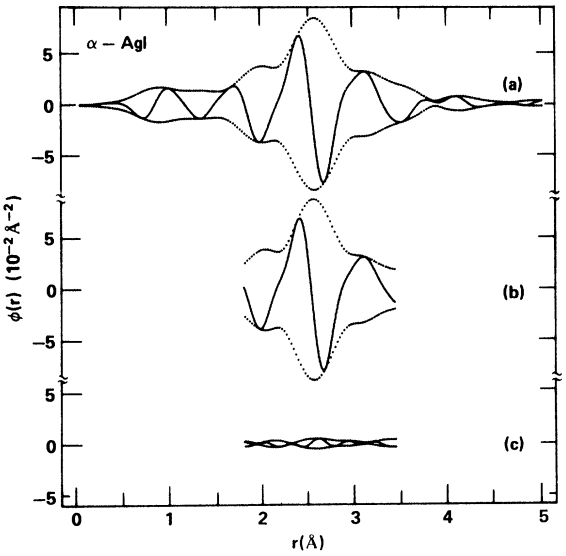

FIG. 6. Data (a) and simulation (b) for the EXAFS in real space on superionic α-AgI at 198 °C. The simulation was obtained as described in the text using the softened hard-sphere model. The difference (c) between the data and the model corresponds to $R = 2.0\%$.

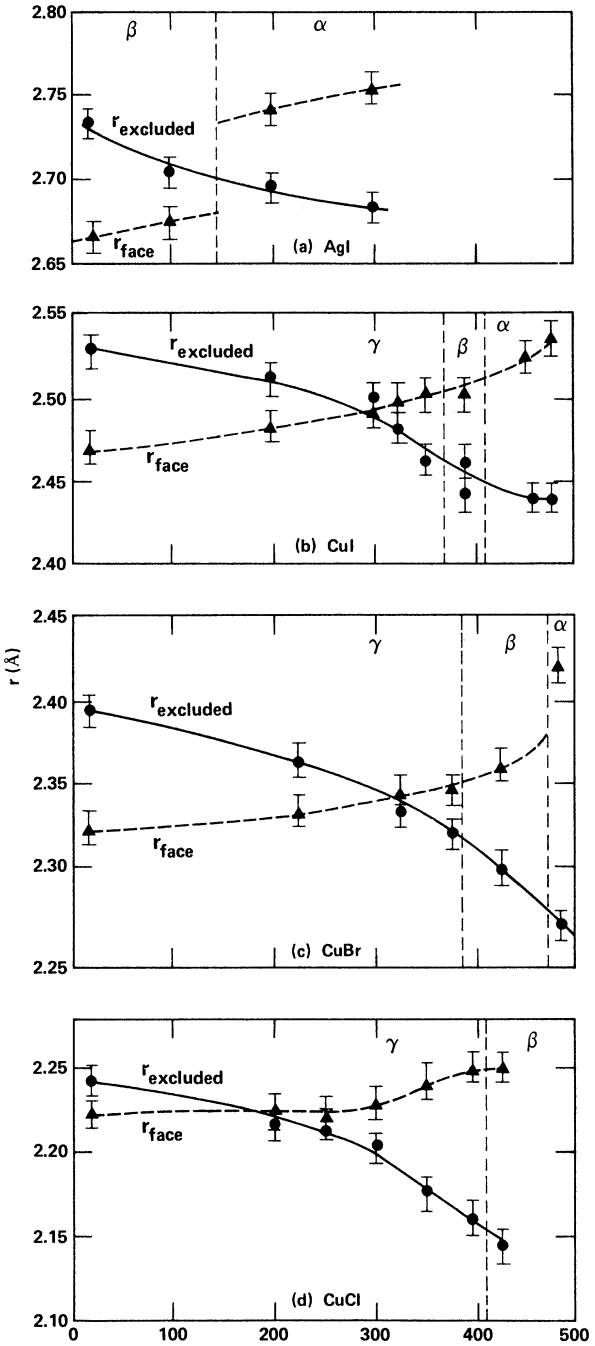

FIG. 7. Hard-sphere radius r_{excluded} obtained from a fit of the excluded-volume model to the EXAFS data on (a) AgI, (b) CuI, (c) CuBr, and (d) CuCl. Also included is r_{face}, the near-neighbor cation-anion distance for a cation in the tetrahedral face. Note that r_{excluded} becomes less than r_{face} when the ionic conductivity becomes large. Also note the differences in the variation of the parameters for AgI and the cuprous halides. The sharp change for AgI is reflected in the sharp discontinuity in the ionic conductivity, whereas the smoother variation for the cuprous halide parameters is reflected in the smoother variation observed in their conductivity.

thermore, each tetrahedral void shares faces with four other tetrahedra in this bcc structure. The Ag ions are allowed to flow easily through these multiply-connected tetrahedral regions. This is expected to yield a high conductivity with little activation energy, as observed ($U \simeq 0.05$ eV $\simeq k_B T$).[16,17] It is interesting to note that the sharp transition from normal to superionic behavior is driven by the increase in r_{face} resulting from the hcp to bcc structural change in the iodine lattice, rather than by an unusual decrease in the r_{excluded}. These rather qualitative conclusions regarding the conduction process have been borne out in a detailed calculation of the dc ionic conductivity in AgI and the copper halides.[53]

The resulting pair-correlation function is asymmetric, as demanded by the data. The trends in $p_{\text{Ag-I}}(r)$ are shown in Fig. 8. At 77 K it is a narrow Gaussian with $\epsilon \approx 0.06$ Å. At room temperature in the β phase it has broadened and become somewhat asymmetric. At 198 °C in the superionic α phase, the width and asymmetry are more pronounced, with a long tail extending to large near-neighbor spacing. This corresponds to the Ag ion density flowing out of one tetrahedral location into another, and becoming large in the region in between, namely, the trigonal sites.

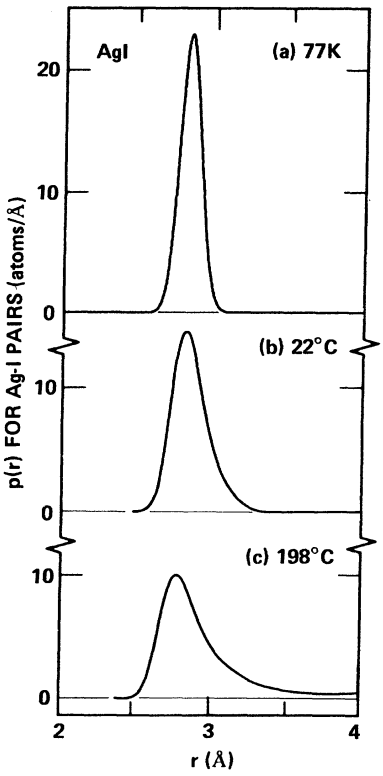

FIG. 8. First-neighbor pair-correlation function for AgI at (a) 77 K, (b) 22°C, and (c) 198 °C. The narrow Gaussian of width 0.06 Å at 77 K becomes broad and asymmetric at elevated temperatures. This trend is described by the excluded-volume model.

As expected, the nearest-neighbor distributions deduced from measurements of Bragg scattering have been shown to be uniformly too broad to explain the EXAFS data, which measure this distribution directly. This broadening includes effects which do not broaden the EXAFS, such as long-wavelength acoustic phonons and certain types of static disorder. To the extent that the nearest-neighbor distribution in particular is desired, an EXAFS measurement is the more direct approach.

VI. EXPERIMENTAL RESULTS AND DISCUSSION FOR THE CUPROUS HALIDES

EXAFS measurements were performed on the Cu K edge of CuCl, CuBr, and CuI as a function of temperature from 77 K up into the superionic phases.[20,41,43] The 77 K data served as the structural standard. At this temperature, all three materials have the cubic zinc-blende structure in which the Cu ions reside at the center of a halogen tetrahedron. In this case, the nearest-neighbor pair-correlation function $p_{\text{Cu-X}}(r)$ is a narrow Gaussian with 4 halogen nearest neighbors centered at r_{tet} (2.34 Å for CuCl, 2.46 Å for CuBr, and 2.61 Å for CuI). The width is estimated to be approximately 0.06 Å from our fit to the 77 K data on CuCl using calculated phase shifts and backscattering amplitude.[32] A width of 0.06 Å has also been obtained for CuBr at 77 K.[54] Four structural models were tested on the data at higher temperatures: the harmonic model or a single Gaussian peak, the displaced-site model or two-Gaussian peak, the anharmonic model, and the excluded-volume model.

A. CuI

We detail the results for these structural models using the EXAFS data on CuI at 470 °C in the superionic α phase as an example. Similar results were obtained for the data at all other temperatures studied.

(1) The single Gaussian peak did not fit well. This is to be expected since the Cu ion vibrations cannot be described by a harmonic oscillator in this superionic phase. If the number of near neighbors N is fixed at 4 corresponding to Cu occupying the tetrahedral site in the fcc iodine lattice, then a fit to the data yields $R = 6.9\%$ for the parameters shown in Table II. The near-neighbor spacing of 2.59 Å is considerably less than that for the center of the tetrahedron ($r_{\text{tet}} = 2.67$ Å from the known lattice constant $a_0 = 6.16$ Å). If N is allowed to vary to minimize R, the fit im-

proves only to $R = 3.5\%$ for $N = 2.22$. The harmonic model does not yield consistent values of N and r_0, and is therefore not appropriate for superionic α-CuI.

(2) In the displaced-site model, $p_{\text{Cu-I}}(r)$ is described by the sum of two Gaussians. Such an approach, proposed by Miyake *et al.*[39] and Buhrer and Halg,[40] has the Cu ions in α-CuI statistically distributed over the four metastable sites that are displaced from the center of a tetrahedron at $(\frac{1}{4}, \frac{1}{4}, \frac{1}{4})$ in the four $\langle 111 \rangle$ directions toward tetrahedral faces. Buhrer and Halg,[40] for example, find a fit to their diffraction data in the α phase at 445 °C with the Cu displaced to (0.3, 0.3, 0.3) and a lattice constant of 6.16 Å. The corresponding near neighbor $p_{\text{Cu-I}}(r)$ consists of the superposition of two Gaussian peaks, one centered at $r_1 = 2.54$ Å with an amplitude of three iodine ions and the other at $r_2 = 3.21$ Å with an amplitude of one iodine neighbor. The Gaussian widths were allowed to differ, corresponding to asymmetric vibrations about this displaced site, and were adjusted to minimize R. This particular model yielded $R = 7.9\%$ for the EXAFS data. A generalization of this model in which the displacement of the Cu ions in the $\langle 111 \rangle$ direction is adjusted as well as the Gaussian widths yielded an improvement in R to 4.2% by narrowing the distribution (see Table II). This class of models did not fit the data well, as seen from the resulting parameters in Table II.

(3) The anharmonic-oscillator model was proposed for α-CuI by Matsubara.[49] The potential in the γ and α phases where the iodine forms an fcc cage is taken to be of the form of Eq. (16), where a and b are temperature-dependent parameters. Matsubara obtained expressions for a and b from the diffraction and specific-heat data of Miyake *et al.*[39] With these specific parameters ($a_{\text{Cu}} = 1.8 \times 10^{-12}$ erg Å^{-2} and $b_{\text{Cu}} = 1.5 \times 10^{-12}$ erg Å^{-3} at 470 °C), a good fit to the EXAFS data could not be obtained ($R = 13.5\%$). A generalization of this anharmonic-oscillator model, in which a and b are adjusted for a best fit, yielded $R = 4.6\%$. The resulting spring constants a and b are approximately twice those determined from the diffraction results.[39] This corresponds to a substantially more narrow distribution, as expected. This anharmonic model with terms up to third order still does not fit the data, however, because it is not sufficiently anharmonic. It does not provide a good approximation to the hard-sphere repulsion, the first term of Eq. (14). This term is important for the superionic conductors since the ions closely approach one another as the mobile ions move through the immobile-ion lattice. The excluded-volume model treats this term as the dominant interaction and therefore yields a good fit to the data.

(4) For applications of the excluded-volume model to fcc structures such as α-CuI, three parameters are needed: r_{excluded} and ϵ, as for bcc structures, and the concentration of Cu ions in the octahedral site, c_{oct}. The Cu ion distributions *within* the tetrahedral and octahedral volumes are determined by the softened hard-sphere interaction. For α-CuI at 470 °C, this yields $R = 1.8\%$ for $r_{\text{excluded}} = 2.44$ Å, $c_{\text{oct}} = 30\%$, and $\epsilon = 0.08$ Å, as shown in Table II. This R is significantly better than the values of $R > 3.5\%$ obtained for the other models tested (as is the case at all temperatures studied). The parameters r_{excluded} and c_{oct} determined from the EXAFS data are shown in Figs. 7(b) and 9(a), respectively. Also included in Fig. 7(b) is r_{face}, the near-neighbor Cu–I spacing for a Cu ion at the center of the face shared by a tetrahedron and octahedron, obtained from the lattice constant. From these figures, it is seen that the concentration of the Cu ions in the octahedral sites begins to increase when r_{excluded} becomes less than r_{face}, allowing easy passage through that face. This is also the temperature

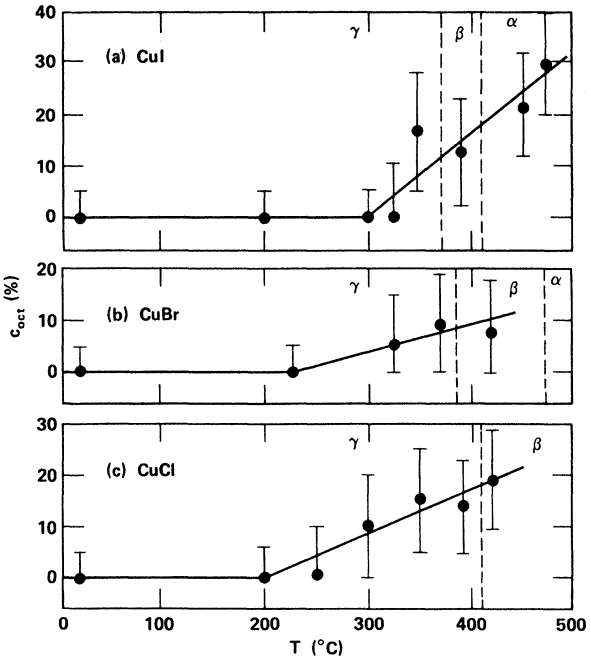

FIG. 9. Concentration of Cu ions in the octahedral sites versus temperature obtained from a fit of the excluded-volume model to the EXAFS data of (a) CuI, (b) CuBr, and (c) CuCl. Note that c_{oct} becomes significant when the ionic conductivity becomes large. Also note the similarity in the variation of c_{oct} for all three materials. Since the structure is bcc for α-CuBr, c_{oct} is not needed as a third parameter.

region where the ionic conductivity (see Fig. 1) becomes significant [i.e., $\approx 10^{-3}$ $(\Omega\,\mathrm{cm})^{-1}$]. These results are in agreement with the conduction path consisting of alternating tetrahedral and octahedral locations, passing through the shared faces.[52]

An example of the pair-correlation functions is shown above in Fig. 5. The narrow, symmetric Gaussian peak at 77 K [Fig. 5(a)] changes substantially on heating the sample to 300 °C [Fig. 5(b)] and even further on going into the superionic phase [Fig. 5(c)]. The peak broadens and the maximum actually shifts inward despite the expansion of the lattice. A long tail at high r develops, due in part to the substantial octahedral occupation, giving rise to a broad and asymmetric peak at 470 °C. The excluded-volume model accounts for all these features. From Fig. 5 it is seen that there is substantial Cu ion density at the bridging trigonal site, which further supports the conclusion that the conduction path consists of alternating tetrahedral and octahedral sites, passing through the shared faces. It should be mentioned further than the increase in $p_{\mathrm{Cu\text{-}I}}(r)$ in this region could not be fully accounted for by placing the Cu ions in the tetrahedral sites only. Octahedral occupation is required to obtain a good fit to the data. For example, for CuI at 470 °C, the R of 2.5% with $c_{\mathrm{oct}}=0$ improved to 1.8% for $c_{\mathrm{oct}}=30\%$. In addition, c_{oct} determined in the least-squares fit to the data varied in a systematic way with temperature, being zero at low temperatures and increasing monotonically to 30% in the superionic phase as shown in Fig. 9(a).

The substantial octahedral occupation in the superionic phase results, in part, from the large allowed volume in the octahedron. For the determined parameters, one has at 470 °C that the allowed volume of an octahedron η_{oct} is approximately ten times larger than the allowed volume of a tetrahedron η_{tet}. There are, however, twice as many tetrahedral locations (8 per unit cube) as there are octahedral locations (4 per unit cube) in the fcc iodine lattice. The density of the Cu ions is not uniform throughout the voids of the fcc iodine lattice, but is different in the tetrahedral and octahedral locations according to the Boltzmann relation and the energy difference between sites, $\Delta V = V_{\mathrm{oct}} - V_{\mathrm{tet}}$. Using $\rho = N_0 c/\eta$, where N_0 is the total number of Cu ions, one has

$$c_{\mathrm{oct}}/c_{\mathrm{tet}} = c_{\mathrm{oct}}/(1 - c_{\mathrm{oct}}) = (4\eta_{\mathrm{oct}}/8\eta_{\mathrm{tet}})\exp(-\Delta V/k_B T). \tag{22}$$

At 470 °C we obtain $c_{\mathrm{oct}} \approx 0.3$ and $\eta_{\mathrm{oct}}/\eta_{\mathrm{tet}} \approx 10$, so that Eq. (22) yields $\Delta V \approx 0.16$ eV. This is the energy barrier for Cu motion through the lattice and compares favorably with the 0.2-eV activation energy determined from NMR relaxation measurements[55] and ionic conductivity.[56]

B. CuBr

The results on CuBr (Ref. 43) parallel those on CuI and AgI, γ- and β-CuBr being similar to γ- and β-CuI, and α-CuBr similar to α-AgI. The details for the four structural models considered will be sketched using as an example the data on fcc γ-CuBr at 370 °C, the high-temperature end of the γ phase where the ionic conductivity is substantial [i.e., ≈ 0.1 $(\Omega\,\mathrm{cm})^{-1}$].

(1) The harmonic model with the Cu ions in the tetrahedral site (4 neighbors) gave $R = 4.2\%$ for the parameters shown in Table III. The near-neighbor spacing of 2.40 Å is less than that for the tetrahedral center (2.48 Å obtained from the

TABLE III. Parameters obtained for several structural models when adjusted to fit the data on CuBr and CuCl. The uncertainty in the determined distances is 0.01 Å and in the other parameters is ≈10%.

Material	Model	R (%)	N	r_0 (Å)	ϵ (Å)
γ-CuBr	Tet. site		4	2.48	
370 °C	Oct. site		6	2.87	
	Harmonic	4.2	4	2.40	0.15
		3.4	2.7	2.39	0.13
	Displaced site:	3.7	3	2.39	0.13
	⟨111⟩		1	3.13	0.31
	Anharmonic	3.0	(see text)		
	Excluded volume	1.1	($r_{\mathrm{excluded}}=2.31$, $c_{\mathrm{oct}}=9\%$)		
γ-CuCl	Tet. site		4	2.36	
393 °C	Oct. site		6	2.73	
	Harmonic	6.3	4	2.32	0.17
		5.6	2.88	2.31	0.14
	Displaced site:	3.7	3	2.30	0.14
	⟨111⟩		1	2.68	0.21
	Anharmonic	3.8	(see text)		
	Excluded volume	0.6	($r_{\mathrm{excluded}}=2.16$, $c_{\mathrm{oct}}=14\%$)		

lattice constant at 370 °C, $a_0 = 5.74$ Å). If N is allowed to vary, the fit improved to $R = 3.4\%$ for 2.70 neighbors. Neither of these single Gaussian fits are particularly good, indicating that the harmonic approximation is inapplicable.

(2) The displaced-site model has been discussed by Hoshino[42] and by Buhrer and Halg[40] for the γ phase. We have tried a displacement from the tetrahedral center in the ⟨111⟩ direction toward the tetrahedral face along the expected conduction path in this fcc Br lattice. This displacement results in a $p_{\text{Cu-Br}}(r)$ that is the sum of two Gaussians whose amplitudes are in the ratio 3:1. A fit to the EXAFS data gave $R = 3.7\%$ for the parameters shown in Table III. This rather poor fit indicates that such a displaced-site model is not appropriate for γ-CuBr. Buhrer and Halg[40] also found that the displaced-site model yielded little improvement in a fit to their neutron-diffraction results on γ- and β-CuBr.

(3) The anharmonic oscillator model has been applied to γ-CuBr by Harada *et al.*[50] A potential for the Cu ions of the form of Eq. (16) was used and the values of the parameters obtained are $a_{\text{Cu}} = 0.94 \times 10^{-12}$ erg Å^{-2} and $b_{\text{Cu}} = 0.5 \times 10^{-12}$ erg Å^{-3}. This potential gave $R = 26\%$ for the EXAFS data. If the potential parameters are allowed to vary, a best fit is obtained for a and b increased by a factor of 4 ($R = 3.0\%$). The corresponding nearest-neighbor distribution is only one-half as broad, as expected. This substantial improvement is still not a good fit, indicating that the anharmonic-oscillator model with up to cubic terms does not describe the structure of CuBr at elevated temperatures.

(4) The excluded-volume model did fit well.[43] The values obtained at 370 °C are $R = 1.1\%$ with $r_{\text{excluded}} = 2.31$ Å, $\epsilon = 0.10$ Å, and $c_{\text{oct}} = 9\%$. This value of R is substantially better than the values of $R > 3\%$ for the other models discussed above. This situation was repeated for the data at the other temperatures studied. The parameters r_{excluded} and c_{oct} determined from these fits are shown in Figs. 7(c) and 9(b), respectively. The same trends seen in γ- and β-CuI are observed in γ- and β-CuBr with a similar relationship between the parameters and the ionic conductivity. α-CuBr, having a bcc Br lattice, differs from α-CuI in that c_{oct} is not included as one of the parameters since the hard-core repulsion alone accounts for the occupation of the various voids in the bcc lattice. This is not the case for the fcc lattice of α-CuI where c_{oct} must be introduced as discussed above.

C. CuCl

For γ- and β-CuCl,[43] the results are similar to those on the γ and β phases of CuBr and CuI. We sketch the results for the four structural models using γ-CuCl at 393 °C where the discrepancies between the models are dramatic.

(1) For the harmonic-oscillator model with Cu in a tetrahedral site, we obtain $R = 6.3\%$ with $N = 4$. The near-neighbor spacing of 2.32 Å is less than the value of $r_{\text{tet}} = 2.36$ Å obtained from lattice constant ($a_0 = 5.46$ Å at 393 °C). If N is allowed to vary, this fit improves slightly to $R = 5.6\%$ for $N = 2.88$ (see Table III). The harmonic model can be ruled out for CuCl at elevated temperatures.

(2) A displaced-site model has been applied to γ-CuCl by Sakata *et al.*[44] and Schreurs *et al.*[45] They use a ⟨111⟩ displacement of the Cu ions from the tetrahedral site. Our best fit for such a displacement to CuCl EXAFS data yields $R = 3.7\%$ (see Table III). This model does not fit well.

(3) The anharmonic model has been applied to γ-CuCl by Sakata *et al.*,[44] by Schreurs *et al.*,[45] and by Valvoda and Jecny.[51] The first group finds that the anharmonic model and the displaced-site model are indistinguishable, but favors the anharmonic approach since it fits their neutron-diffraction data at all temperatures up to 300 °C with no additional parameters. They obtain for the Cu ion potential parameters of Eq. (16) the values $a_{\text{Cu}} = 0.74 \times 10^{-12}$ erg Å^{-2} and $b_{\text{Cu}} = 0.6 \times 10^{-12}$ erg Å^{-3}. This potential does not fit the EXAFS data, giving $R = 25\%$. If the parameters of the anharmonic model are allowed to vary, a least-squares fit gives $R = 3.8\%$ with spring constants that are 4 times stiffer than those deduced from diffraction, as expected. This is an improvement but still not a good fit.

(4) The excluded-volume model did fit the data,[43] yielding $R = 0.6\%$ for $r_{\text{excluded}} = 2.16$ Å, $\epsilon = 0.07$ Å, and $c_{\text{oct}} = 14\%$. This fit is substantially better than those for the other models, with $R > 3.7\%$. The same was true at the other temperatures studied. The temperature variation of the excluded-volume model parameters for CuCl are shown in Figs. 7(d) and 9(c). The same relationships between the parameters and the ionic conductivity that were observed for CuI and CuBr apply as well to CuCl.

VII. MOBILE ION DENSITY

The excluded-volume model can also be used to obtain charge contour plots according to Eq. (21). The parameters that specify the cation density $\rho_c(\vec{r})$ (i.e., r_{excluded}, ϵ, and c_{oct}) were determined in fits to the data as discussed above and are shown in Figs. 7 and 9. Various cross sections of $\rho_c(\vec{r})$ can then be obtained to vividly illustrate the spreading of the mobile-ion density with increasing temperature and to indicate the

conduction path taken from one site to another. For the bcc materials α-AgI and α-CuBr, the appropriate section is a (100) plane and for the fcc materials, γ-phase cuprous halides and α-CuI, the (110) plane. First consider the bcc materials.

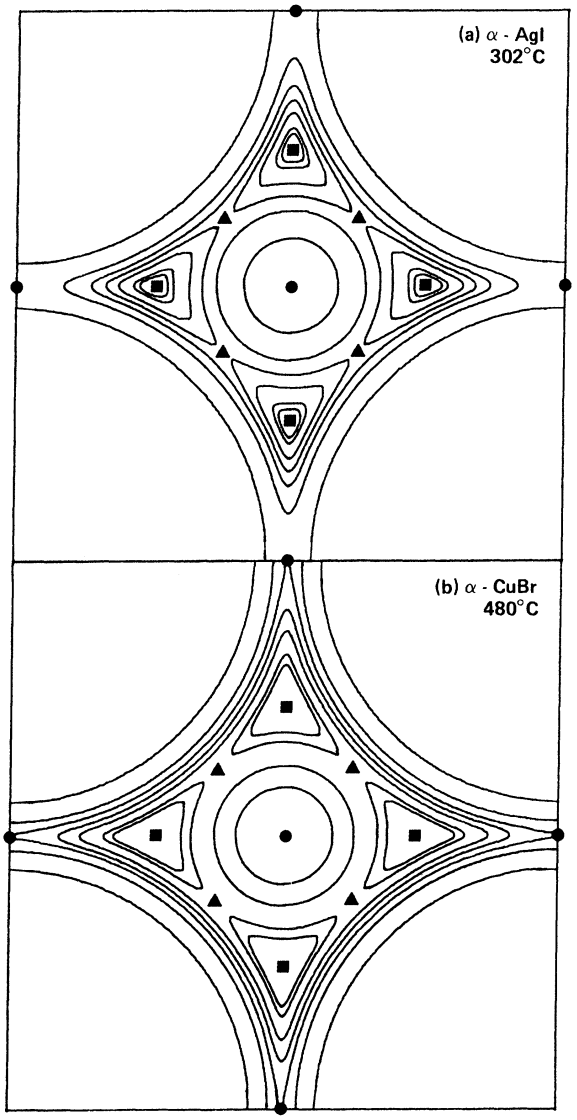

FIG. 10. A contour plot of the cation density in the superionic α phase of (a) AgI at 302 °C and (b) CuBr at 480 °C. The plot is for a (100) plane which includes the conduction path in the ⟨110⟩ directions from one tetrahedron through a trigonal face into another tetrahedron. The various Strock sites are labeled as follows: □, tetrahedral; ○, octahedral; and △, bridging face site. Moving away from the tetrahedral centers, the contours correspond to $\rho/\rho_0 = 0.95, 0.9, 0.7, 0.5, 0.3, 0.1$, and ≈ 0. Note that the cation density peaks at the tetrahedral sites but also spreads substantially through the tetrahedral faces.

Figure 10 displays the cation density on the face of the bcc unit cell of superionic α-AgI at 302 °C and α-CuBr at 480 °C. While the contours are similar, they differ in that the Cu density in CuBr is more spread out than that for Ag in AgI, possibly due to the higher temperature of the CuBr. The plot is of the (100) plane where the anions occupy the corners of the square and the positions above and below the center of the square. The Strock sites[2] are labeled by the symbols as noted. It is seen that the cation density peaks at the tetrahedral sites but is also substantial at the bridging trigonal sites. The easy conduction path is along the ⟨110⟩ directions from one tetrahedron to another through the shared faces. The charge density at the octahedral site is lower than that for the trigonal site, indicating that the ⟨100⟩ direction is a less probable path for conduction.

Using this determined density and the Boltzmann relation, Eq. (13), one can estimate the potential-energy barrier heights for conduction in different directions. Consider α-AgI. The distorted tetrahedral site is the lowest-energy site for Ag ions in this iodine bcc cage. From Eq. (13), the trigonal site is higher in energy by about 0.04 eV while the octahedral site is higher by about 0.18 eV. The 0.04-eV barrier for conduction along the ⟨110⟩ direction is close to the 0.05-eV conductivity activation energy.[17] For conduction along the ⟨100⟩ direction, as suggested by Flygare and Huggins,[48] the barrier is approximately 0.18 eV. This is nearly 5 times larger than the barrier along the ⟨110⟩ direction, indicating that conduction in the ⟨100⟩ direction is substantially less favorable.

It is interesting to compare the Ag charge distribution shown in Fig. 10(a) with the qualitatively similar distribution which has been extracted from neutron-diffraction measurements on single-crystal α-AgI at 300 °C by Cava *et al.*[9] [see Fig. 1(c) in that work]. The ratio of ρ at a trigonal site to that at a tetrahedral site ρ_0 is in agreement for the two studies, being about 0.5. On the other hand, our results show a generally narrower distribution of the Ag ion density, and a more abrupt decrease in it as an iodine ion is approached. This is reflected in the different densities at the octahedral site: $\rho/\rho_0 \approx 0.05$ from the EXAFS and about 0.3 from the neutron data. We expect that our independent particle model will tend to underestimate ρ at those points where cooperative Ag–I motions are likely to be important, such as the octahedral site. Thus our value of 0.05 might be best viewed as a lower bound. Another measure of ρ comes from molecular dynamics (MD) calculations, which *do* include cooperative effects. Vashishta and Rahman[57]

find $\rho/\rho_0 \approx 0.17$ at the octahedral site in their MD calculation of α-AgI. We have reasoned elsewhere[58] that the MD calculation tends to overestimate ρ in the region near an anion. Accordingly, we expect that the actual ρ/ρ_0 lies somewhere between 0.05 and 0.17 at the octahedral site, significantly below the neutron result of 0.3.

Next we consider the cation density in the fcc materials. In Fig. 11 is displayed the Cu ion density in the (110) plane of the iodine fcc lattice of CuI at 470 °C. The entire unit cube is shown with iodine ions occupying six positions around the edge of the rectangle and four positions above and below the interior of the rectangle. The various sites are labeled. Figure 12 shows the bottom half of this unit cube at four increasing temperatures for CuI. The dramatic spreading of the Cu density with increasing temperature is clearly evident in Fig. 12. At room temperature [Fig. 12(a)] only the tetrahedral sites are occupied. At this temperature CuI has the zinc-blende structure, so only alternate tetrahedral sites are occupied (T_d^2). As a result only that half of the unit cube with the occupied sites is shown in Fig. 12(a). Since our EXAFS analysis considered only nearest neighbors, the difference between alternate tetrahedral sites being occupied (T_d^2) and all the tetrahedral sites being occupied (O_h^5) could not be distinguished. For this we rely on the results of diffraction studies.[40] At 350 °C [Fig. 12(c)], lobes of Cu ion density have entered the octahedral site ($c_{oct} = 9\%$) and are even more substantial in the superionic α phase at 470 °C [Fig. 12(d)] where $c_{oct} = 30\%$. In the α phase the tetrahedral sites are equally occupied (O_h^5),[40] and we use this fact to display the contours of Fig. 11.

Using this determined density of Figs. 11 and 12 and the Boltzmann relation, we can estimate the barrier heights for conduction along various directions. Consider α-CuI at 470 °C (Fig. 11). The tetrahedral site is the lowest-energy site. Along the ⟨111⟩ direction from one tetrahedron to another through an octahedron, the octahedral site is a local minimum in density. This difference in density yields a barrier height for conduction in the ⟨111⟩ direction of approximately 0.16 eV, which compares favorably with the 0.2-eV activation energy from NMR (Ref. 55) and conductivity.[56] It should be noted that the density is very small at $(\frac{1}{4}, \frac{1}{4}, 0)$, the edge of the tetrahedron shared with an octahedron. The activation barrier for this site is approximately 0.7 eV, substantially larger than the barrier at the tetrahedral face. This implies that the viable conduction path is in a ⟨111⟩ direction through a face into an octahedron, not in a ⟨100⟩ direction through a tetrahedral edge.

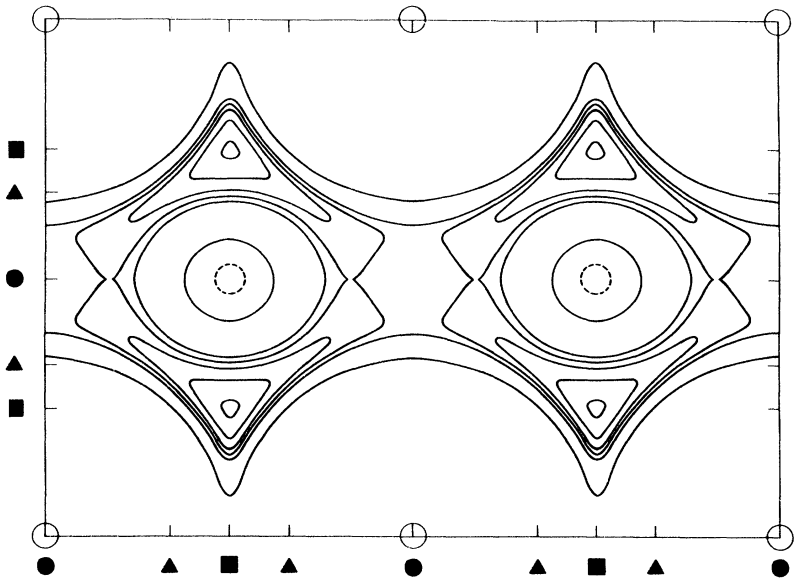

FIG. 11. Contour plot of the Cu ion density in the superionic α phase of CuI at 470 °C. The plot is for the (110) plane which includes a conduction path in a ⟨111⟩ direction from one tetrahedron through an octahedron, into another tetrahedron. The various sites are labeled along the boundaries as follows: □ , tetrahedral; ○, octahedral; and △, bridging face site. Moving away from the tetrahedral centers, the contours correspond to $\rho/\rho_0 = 0.95$, 0.5, 0.2, 0.1, 0.05, and ≈ 0. Note that the Cu ion density peaks at the tetrahedral sites but also spreads through the tetrahedral faces into the octahedral regions.

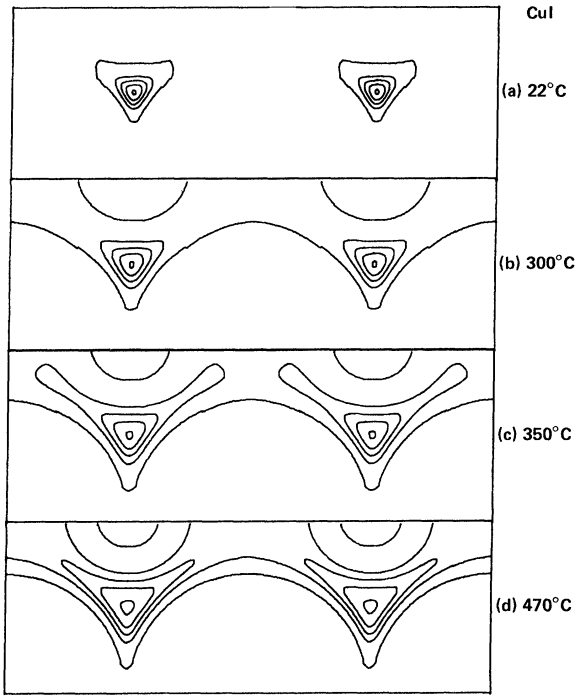

FIG. 12. Contour plot of the Cu ion density in the (110) plane of CuI in the γ phase at (a) 22 °C, (b) 300 °C, and (c) 350 °C, and in the superionic α phase at (d) 470 °C. The plot is for the (110) plane which includes a conduction path in a ⟨111⟩ direction from one tetrahedron through an octahedron, into another tetrahedron. Moving away from the tetrahedral sites, the contours correspond to $\rho/\rho_0 = 0.95, 0.5, 0.2, 0.05$, and ≈ 0. Note that the Cu ion density peaks at the tetrahedral sites but also spreads through the tetrahedral faces into the octahedral regions.

VIII. SUMMARY

The EXAFS data on AgI and the cuprous halides from low temperatures up into the superionic phases have been analyzed using four structural models: harmonic oscillator, displaced site, anharmonic oscillator, and excluded volume. The most satisfactory description of the EXAFS structural information is obtained with the excluded-volume model. In this model the actual ionic pair potential is approximated by a softened hard-sphere interaction which, in turn, determines the near-neighbor pair-correlation function. The results indicate that the tetrahedral locations in the halogen lattice are preferred by the mobile cations but that substantial density occurs at the trigonal sites at elevated temperatures. For the bcc materials, α-AgI and α-CuBr, this indicates that the mobile ions move in ⟨110⟩ directions through the face-shared tetrahedra. For the fcc materials, α-CuI and γ-cuprous halides, significant octahedral occupation was also found at elevated temperatures. The indicated conduction path in these cases is in the ⟨111⟩ directions through the faces shared by the tetrahedra and octahedra in the fcc halogen lattice.

The structural results also yield some insight into the transition to the superionic phase. For AgI where the ionic conductivity increases sharply by 4 orders of magnitude at the β to α transition, there is an abrupt opening of the tetrahedral face allowing the Ag ions to move into neighboring locations. For the cuprous halides, on the other hand, where the conductivity increases more gradually, there is a more gradual change in the structural parameters.

In addition to determining the conduction direction from the structural results, one can also estimate the potential-energy barrier heights from the ion density using the Boltzmann relation. For example, in α-AgI the trigonal site presents a barrier of about 0.04 eV while the octahedral site a barrier of about 0.18 eV. Conduction through the trigonal site in ⟨110⟩ directions is preferred, with an activation energy of approximately 0.04 eV, in good agreement with the 0.05 eV from conductivity studies. In α-CuI the octahedral site presents a barrier of about 0.16 eV while the tetrahedral edge a barrier of 0.7 eV. Conduction through the octahedra in the ⟨111⟩ directions is preferred, with an activation energy of 0.16 eV in agreement with the 0.2 eV from conductivity and NMR.

We have also pointed out the differences in the nature of the structural information probed using the two techniques: diffraction and EXAFS. The charge-density distributions obtained from Bragg scattering are dominated by long-range correlations. Consequently, they are broadened by thermal vibrations which do not affect nearest-neighbor atoms, such as long-wavelength acoustic modes. A nearest-neighbor distribution inferred from Bragg scattering will reflect this broadening. EXAFS data, on the other hand, is dominated by the near-neighbor correlations. This yields substantially narrower distributions which reflect the details of the short-range pairwise interactions. The information on superionic conduction which has been gained in this work can be attributed to the ability of EXAFS to probe these interactions.

ACKNOWLEDGMENTS

We wish to acknowledge the contributions of W. Stutius in the early stages of this work. Some

of the materials incorporated in this work were developed at the Stanford Synchrotron Radiation Laboratory which is supported by the National Science Foundation (under Contract No. DMR77-27489), in cooperation with SLAC and the Department of Energy.

[1]Several review articles have appeared recently: (a) *Solid Electrolytes*, Vol. XXI of *Topics in Applied Physics*, edited by S. Geller (Springer, Berlin, 1977); (b) *Solid Electrolytes: General Principles, Characterization, Materials, Applications*, edited by P. Hagenmuller and W. von Gool (Academic, New York, 1977); (c) J. B. Boyce and B. A. Huberman, Phys. Rep. 51, 189 (1979); (d) *Physics of Superionic Conductors*, Vol. XV of *Topics in Current Physics*, edited by M. B. Salamon (Springer-Verlag, Berlin, 1979); (e) *Fast Ion Transport in Solids*, edited by P. Vashishta, J. N. Mundy, and G. K. Shenoy (North-Holland, New York, 1979).

[2]L. W. Strock, Z. Phys. Chem. Abt. B 25, 411 (1934); 31, 132 (1936).

[3]S. Hoshino, J. Phys. Soc. Jpn. 12, 315 (1957).

[4]G. Burley, J. Chem. Phys. 38, 2807 (1963).

[5]W. Buhrer and W. Halg, Helv. Phys. Acta 47, 27 (1974).

[6]A. F. Wright and B. E. F. Fender, J. Phys. C 10, 2261 (1977).

[7]G. Eckold, K. Funke, J. Kalus, and R. E. Lechner, J. Phys. Chem. Solids 37, 1097 (1976), and references contained therein.

[8]J. B. Boyce, T. M. Hayes, W. Stutius, and J. C. Mikkelsen, Jr., Phys. Rev. Lett. 38, 1362 (1977).

[9]R. J. Cava, F. Reidinger, and B. J. Wuensch, Solid State Commun. 24, 411 (1977).

[10]M. Suzuki and H. Okazaki, Phys. Status Solidi A 42, 133 (1977).

[11]S. Hoshino, T. Sakuma, and Y. Fujii, Solid State Commun. 22, 763 (1977).

[12]J. B. Boyce and J. C. Mikkelsen, Jr., Solid State Commun. 31, 741 (1979).

[13]For a discussion of the various types of transitions and a list of materials in each category, see Ref. 1(c).

[14]M. O'Keeffe and B. G. Hyde, Philos. Mag. 33, 219 (1976) and references therein.

[15]B. A. Huberman, Phys. Rev. Lett. 32, 1000 (1974).

[16]H. Hoshino and M. Shimoji, J. Phys. Chem. Solids 35, 321 (1974).

[17]A. Kvist and A. M. Josefson, Z. Naturforsch. 23A, 625 (1968); H. Hoshino, S. Makino, and M. Shimoji, J. Phys. Chem. Solids 35, 667 (1974); R. N. Schock and E. Hinze, J. Phys. Chem. Solids 36, 713 (1975); P. C. Allen and D. Lazarus, Phys. Rev. B 17, 1913 (1978).

[18]J. B. Wagner and C. Wagner, J. Chem. Phys. 26, 1597 (1957) and references contained therein; T. Jow and J. B. Wagner, J. Electrochem. Soc. 125, 613 (1978).

[19]For a discussion of EXAFS with references to earlier work see the review by T. M. Hayes, J. Non-Cryst. Solids 31, 57 (1978).

[20]For a discussion of EXAFS and applications to superionic conductors see J. B. Boyce and T. M. Hayes, in *Physics of Superionic Conductors*, Ref. 1(d), Chap. 2.

[21]See, for example, Y. Tsuchiya, S. Tamaki, Y. Waseda, and J. M. Toguri, J. Phys. C 11, 651 (1978) and T. Sakuma, *ibid.* 11, L747 (1978).

[22]G. Beni and P. M. Platzman, Phys. Rev. B 14, 1514 (1976).

[23]J. C. Mikkelsen, Jr., J. B. Boyce, and R. Allen, Rev. Sci. Instrum. 51, 388 (1980).

[24]B. M. Kincaid, SSRP Report No. 75/03 (unpublished).

[25]See, for example, M. Brown, R. E. Peierls, and E. A. Stern, Phys. Rev. B 15, 738 (1977).

[26]D. E. Sayers, E. A. Stern, and F. W. Lytle, Phys. Rev. Lett. 27, 1204 (1971).

[27]E. A. Stern, Phys. Rev. B 10, 3027 (1974).

[28]C. A. Ashley and S. Doniach, Phys. Rev. B 11, 1279 (1975).

[29]P. A. Lee and J. B. Pendry, Phys. Rev. B 11, 2795 (1975).

[30]T. M. Hayes, P. N. Sen, and S. H. Hunter, J. Phys. C 9, 4357 (1976).

[31]P. A. Lee and G. Beni, Phys. Rev. B 15, 2862 (1977).

[32]B.-K. Teo and P. A. Lee, J. Am. Chem. Soc. 101, 2815 (1979).

[33]S. J. Gurman and J. B. Pendry, Solid State Commun. 20, 287 (1976).

[34]See, for example, F. W. Lytle, D. E. Sayers, and E. A. Stern, Phys. Rev. B 11, 4825 (1975).

[35]N. F. Mott and H. S. W. Massey, *The Theory of Atomic Collisions*, 3rd ed. (Clarendon, Oxford, 1965), p. 562.

[36]P. H. Citrin, P. Eisenberger, and B. M. Kincaid, Phys. Rev. Lett. 36, 1346 (1976).

[37]P. Eisenberger and G. S. Brown, Solid State Commun. 29, 481 (1979).

[38]T. M. Hayes and J. B. Boyce (unpublished).

[39]S. Miyake, S. Hoshino, and T. Takenaka, J. Phys. Soc. Jpn. 7, 19 (1952).

[40]W. Buhrer and W. Halg, Electrochim. Acta 22, 701 (1977).

[41]J. B. Boyce, T. M. Hayes, J. C. Mikkelsen, Jr., and W. Stutius, Solid State Commun. 33, 183 (1980).

[42]S. Hoshino, J. Phys. Soc. Jpn. 7, 560 (1952).

[43]J. B. Boyce, T. M. Hayes, and J. C. Mikkelsen, Jr., Solid State Commun. 35, 237 (1980).

[44]M. Sakata, S. Hoshino, and J. Harada, Acta Crystallogr. A 30, 655 (1974).

[45]J. Schreurs, M. H. Mueller, and L. H. Schwartz, Acta Crystallogr. A 32, 618 (1976).

[46]T. M. Hayes, J. B. Boyce, and J. L. Beeby, J. Phys. C 11, 2931 (1978).

[47]For a review of the molecular dynamics work, see the papers in Ref. 1(e) by A. Rahman, p. 643, W. Schommers, p. 625, and P. Vashishta and A. Rahman, p. 527.

[48]W. H. Flygare and R. A. Huggins, J. Phys. Chem. Solids 34, 1199 (1973).

[49]T. Matsubara, J. Phys. Soc. Jpn. 38, 1076 (1975).

[50]J. Harada, H. Suzuki, and S. Hoshino, J. Phys. Soc. Jpn. 41, 1707 (1976).

[51]V. Valvoda and J. Jecny, Phys. Status Solidi A 45, 269 (1978).

[52]L. V. Azaroff, J. Appl. Phys. 32, 1658 (1961).

[53]T. M. Hayes and J. B. Boyce, Phys. Rev. B 21, 2513 (1980).
[54]B. Bunker (private communication).
[55]J. B. Boyce and B. A. Huberman, Solid State Commun. 21, 31 (1977).
[56]W. Jost, *Diffusion in Solids, Liquids and Gases* (Academic, New York, 1960), p. 188.
[57]P. Vashishta and A. Rahman, Ref. 1(e), p. 527.
[58]T. M. Hayes and J. B. Boyce, J. Phys. C 13, L731 (1980).